This is the accepted manuscript made available via CHORUS. The article has been published as:

Measurement of the W→eν and Z/γ^{*}→e^{+}e^{-} production cross sections at mid-rapidity in proton-proton collisions at sqrt[s]=500 GeV

L. Adamczyk *et al.* (STAR Collaboration)

Phys. Rev. D **85**, 092010 — Published 16 May 2012

DOI: 10.1103/PhysRevD.85.092010

Measurement of the $W \to e\nu$ and $Z/\gamma^* \to e^+e^-$ Production Cross Sections at Mid-rapidity in Proton-Proton Collisions at $\sqrt{s} = 500$ GeV

L. Adamczyk,[9] G. Agakishiev,[19] M. M. Aggarwal,[30] Z. Ahammed,[48] A. V. Alakhverdyants,[19] I. Alekseev,[17] J. Alford,[20] B. D. Anderson,[20] C. D. Anson,[28] D. Arkhipkin,[2] E. Aschenauer,[2] G. S. Averichev,[19] J. Balewski,[24] Banerjee,[48] Z. Barnovska,[12] D. R. Beavis,[2] R. Bellwied,[44] M. J. Betancourt,[24] R. R. Betts,[8] A. Bhasin,[18] A. K. Bhati,[30] H. Bichsel,[50] J. Bielcik,[11] J. Bielcikova,[12] L. C. Bland,[2] I. G. Bordyuzhin,[17] W. Borowski,[41] J. Bouchet,[20] A. V. Brandin,[27] S. G. Brovko,[4] E. Bruna,[52] S. Bueltmann,[29] I. Bunzarov,[19] T. P. Burton,[2] J. Butterworth,[36] X. Z. Cai,[40] H. Caines,[52] M. Calderón de la Barca Sánchez,[4] D. Cebra,[4] R. Cendejas,[5] M. C. Cervantes,[42] P. Chaloupka,[12] S. Chattopadhyay,[48] H. F. Chen,[38] J. H. Chen,[40] J. Y. Chen,[7] L. Chen,[7] J. Cheng,[45] M. Cherney,[10] A. Chikanian,[52] W. Christie,[2] P. Chung,[12] J. Chwastowski,[9] M. J. M. Codrington,[42] R. Corliss,[24] J. G. Cramer,[50] H. J. Crawford,[3] X. Cui,[38] A. Davila Leyva,[43] L. C. De Silva,[44] R. R. Debbe,[2] T. G. Dedovich,[19] J. Deng,[39] R. Derradi de Souza,[6] S. Dhamija,[16] L. Didenko,[2] F. Ding,[4] A. Dion,[2] P. Djawotho,[42] X. Dong,[23] J. L. Drachenberg,[42] J. E. Draper,[4] C. M. Du,[22] L. E. Dunkelberger,[5] J. C. Dunlop,[2] L. G. Efimov,[19] M. Elnimr,[51] J. Engelage,[3] G. Eppley,[36] L. Eun,[23] O. Evdokimov,[8] R. Fatemi,[21] Fazio,[2] J. Fedorisin,[19] R. G. Fersch,[21] P. Filip,[19] E. Finch,[52] Y. Fisyak,[2] C. A. Gagliardi,[42] D. R. Gangadharan,[28] F. Geurts,[36] S. Gliske,[1] Y. N. Gorbunov,[10] O. G. Grebenyuk,[23] D. Grosnick,[47] S. Gupta,[18] W. Guryn,[2] B. Haag,[4] O. Hajkova,[11] A. Hamed,[42] L-X. Han,[40] J. W. Harris,[52] J. P. Hays-Wehle,[24] S. Heppelmann,[31] A. Hirsch,[33] G. W. Hoffmann,[43] D. J. Hofman,[8] S. Horvat,[52] B. Huang,[2] H. Z. Huang,[5] P. Huck,[7] T. J. Humanic,[28] L. Huo,[42] G. Igo,[5] W. W. Jacobs,[16] C. Jena,[14] J. Joseph,[20] E. G. Judd,[3] S. Kabana,[41] K. Kang,[45] J. Kapitan,[12] K. Kauder,[8] H. W. Ke,[7] D. Keane,[20] A. Kechechyan,[19] A. Kesich,[4] D. Kettler,[50] D. P. Kikola,[33] J. Kiryluk,[23] A. Kisiel,[49] V. Kizka,[19] S. R. Klein,[23] D. D. Koetke,[47] T. Kollegger,[13] J. Konzer,[33] I. Koralt,[29] L. Koroleva,[17] W. Korsch,[21] L. Kotchenda,[27] P. Kravtsov,[27] K. Krueger,[1] L. Kumar,[20] M. A. C. Lamont,[2] J. M. Landgraf,[2] S. LaPointe,[51] J. Lauret,[2] A. Lebedev,[2] R. Lednicky,[19] J. H. Lee,[2] W. Leight,[24] M. J. LeVine,[2] C. Li,[38] L. Li,[43] W. Li,[40] X. Li,[33] X. Li,[39] Y. Li,[45] Z. M. Li,[7] L. M. Lima,[37] M. A. Lisa,[28] F. Liu,[7] T. Ljubicic,[2] W. J. Llope,[36] R. S. Longacre,[2] Y. Lu,[38] X. Luo,[7] A. Luszczak,[9] G. L. Ma,[40] Y. G. Ma,[40] D. P. Mahapatra,[14] R. Majka,[52] O. I. Mall,[4] S. Margetis,[20] C. Markert,[43] H. Masui,[23] H. S. Matis,[23] D. McDonald,[36] T. S. McShane,[10] S. Mioduszewski,[42] M. K. Mitrovski,[2] Y. Mohammed,[42] B. Mohanty,[48] B. Morozov,[17] M. G. Munhoz,[37] M. K. Mustafa,[33] M. Naglis,[23] B. K. Nandi,[15] Md. Nasim,[48] T. K. Nayak,[48] L. V. Nogach,[32] G. Odyniec,[23] A. Ogawa,[2] K. Oh,[34] A. Ohlson,[52] V. Okorokov,[27] E. W. Oldag,[43] R. A. N. Oliveira,[37] D. Olson,[23] P. Ostrowski,[49] M. Pachr,[11] B. S. Page,[16] S. K. Pal,[48] Pan,[5] Y. Pandit,[20] Y. Panebratsev,[19] T. Pawlak,[49] B. Pawlik,[9] H. Pei,[8] C. Perkins,[3] W. Peryt,[49] P. Pile,[2] M. Planinic,[53] J. Pluta,[49] D. Plyku,[29] N. Poljak,[53] J. Porter,[23] A. M. Poskanzer,[23] C. B. Powell,[23] D. Prindle,[50] C. Pruneau,[51] N. K. Pruthi,[30] M. Przybycien,[9] P. R. Pujahari,[15] J. Putschke,[51] H. Qiu,[23] R. Raniwala,[35] S. Raniwala,[35] R. L. Ray,[43] R. Redwine,[24] R. Reed,[4] C. K. Riley,[52] H. G. Ritter,[23] J. B. Roberts,[36] O. V. Rogachevskiy,[19] J. L. Romero,[4] L. Ruan,[2] J. Rusnak,[12] N. R. Sahoo,[48] I. Sakrejda,[23] S. Salur,[23] A. Sandacz,[49] J. Sandweiss,[52] E. Sangaline,[4] A. Sarkar,[15] J. Schambach,[43] R. P. Scharenberg,[33] A. M. Schmah,[23] B. Schmidke,[2] N. Schmitz,[25] T. R. Schuster,[13] J. Seele,[24] J. Seger,[10] P. Seyboth,[25] N. Shah,[5] E. Shahaliev,[19] M. Shao,[38] B. Sharma,[30] M. Sharma,[51] S. S. Shi,[7] Q. Y. Shou,[40] E. P. Sichtermann,[23] R. N. Singaraju,[48] M. J. Skoby,[33] D. Smirnov,[2] N. Smirnov,[52] D. Solanki,[35] P. Sorensen,[2] U. G. deSouza,[37] H. M. Spinka,[1] B. Srivastava,[33] T. D. S. Stanislaus,[47] S. G. Steadman,[24] J. R. Stevens,[16] R. Stock,[13] M. Strikhanov,[27] B. Stringfellow,[33] A. A. P. Suaide,[37] M. C. Suarez,[8] M. Sumbera,[12] X. M. Sun,[23] Y. Sun,[38] Z. Sun,[22] B. Surrow,[24] D. N. Svirida,[17] T. J. M. Symons,[23] A. Szanto de Toledo,[37] J. Takahashi,[6] A. H. Tang,[2] Z. Tang,[38] L. H. Tarini,[51] T. Tarnowsky,[26] D. Thein,[43] J. H. Thomas,[23] J. Tian,[40] A. R. Timmins,[44] D. Tlusty,[12] M. Tokarev,[19] T. A. Trainor,[50] S. Trentalange,[5] R. E. Tribble,[42] P. Tribedy,[48] B. A. Trzeciak,[49] O. D. Tsai,[5] J. Turnau,[9] T. Ullrich,[2] D. G. Underwood,[1] G. Van Buren,[2] G. van Nieuwenhuizen,[24] J. A. Vanfossen, Jr.,[20] R. Varma,[15] G. M. S. Vasconcelos,[6] F. Videbæk,[2] Y. P. Viyogi,[48] S. Vokal,[19] S. A. Voloshin,[51] A. Vossen,[16] M. Wada,[43] F. Wang,[33] G. Wang,[5] H. Wang,[26] J. S. Wang,[22] Q. Wang,[33] X. L. Wang,[38] Y. Wang,[45] G. Webb,[21] J. C. Webb,[2] G. D. Westfall,[26] C. Whitten Jr.,[5] H. Wieman,[23] S. W. Wissink,[16] R. Witt,[46] W. Witzke,[21] Y. F. Wu,[7] Z. Xiao,[45] W. Xie,[33] K. Xin,[36] H. Xu,[22] N. Xu,[23] Q. H. Xu,[39] W. Xu,[5] Y. Xu,[38] Z. Xu,[2] L. Xue,[40] Y. Yang,[22] Y. Yang,[7] P. Yepes,[36] Y. Yi,[33] K. Yip,[2] I-K. Yoo,[34] M. Zawisza,[49] H. Zbroszczyk,[49] J. B. Zhang,[7] S. Zhang,[40] W. M. Zhang,[20] X. P. Zhang,[45] Y. Zhang,[38] Z. P. Zhang,[38] F. Zhao,[5] J. Zhao,[40] C. Zhong,[40] X. Zhu,[45] Y. H. Zhu,[40] and Y. Zoulkarneeva[19]

(STAR Collaboration)

[1] *Argonne National Laboratory, Argonne, Illinois 60439, USA*

[2] *Brookhaven National Laboratory, Upton, New York 11973, USA*
[3] *University of California, Berkeley, California 94720, USA*
[4] *University of California, Davis, California 95616, USA*
[5] *University of California, Los Angeles, California 90095, USA*
[6] *Universidade Estadual de Campinas, Sao Paulo, Brazil*
[7] *Central China Normal University (HZNU), Wuhan 430079, China*
[8] *University of Illinois at Chicago, Chicago, Illinois 60607, USA*
[9] *Krakow Universitiy of Technology, Crakow, Poland*
[10] *Creighton University, Omaha, Nebraska 68178, USA*
[11] *Czech Technical University in Prague, FNSPE, Prague, 115 19, Czech Republic*
[12] *Nuclear Physics Institute AS CR, 250 68 Řež/Prague, Czech Republic*
[13] *University of Frankfurt, Frankfurt, Germany*
[14] *Institute of Physics, Bhubaneswar 751005, India*
[15] *Indian Institute of Technology, Mumbai, India*
[16] *Indiana University, Bloomington, Indiana 47408, USA*
[17] *Alikhanov Institute for Theoretical and Experimental Physics, Moscow, Russia*
[18] *University of Jammu, Jammu 180001, India*
[19] *Joint Institute for Nuclear Research, Dubna, 141 980, Russia*
[20] *Kent State University, Kent, Ohio 44242, USA*
[21] *University of Kentucky, Lexington, Kentucky, 40506-0055, USA*
[22] *Institute of Modern Physics, Lanzhou, China*
[23] *Lawrence Berkeley National Laboratory, Berkeley, California 94720, USA*
[24] *Massachusetts Institute of Technology, Cambridge, MA 02139-4307, USA*
[25] *Max-Planck-Institut für Physik, Munich, Germany*
[26] *Michigan State University, East Lansing, Michigan 48824, USA*
[27] *Moscow Engineering Physics Institute, Moscow Russia*
[28] *Ohio State University, Columbus, Ohio 43210, USA*
[29] *Old Dominion University, Norfolk, VA, 23529, USA*
[30] *Panjab University, Chandigarh 160014, India*
[31] *Pennsylvania State University, University Park, Pennsylvania 16802, USA*
[32] *Institute of High Energy Physics, Protvino, Russia*
[33] *Purdue University, West Lafayette, Indiana 47907, USA*
[34] *Pusan National University, Pusan, Republic of Korea*
[35] *University of Rajasthan, Jaipur 302004, India*
[36] *Rice University, Houston, Texas 77251, USA*
[37] *Universidade de Sao Paulo, Sao Paulo, Brazil*
[38] *University of Science & Technology of China, Hefei 230026, China*
[39] *Shandong University, Jinan, Shandong 250100, China*
[40] *Shanghai Institute of Applied Physics, Shanghai 201800, China*
[41] *SUBATECH, Nantes, France*
[42] *Texas A&M University, College Station, Texas 77843, USA*
[43] *University of Texas, Austin, Texas 78712, USA*
[44] *University of Houston, Houston, TX, 77204, USA*
[45] *Tsinghua University, Beijing 100084, China*
[46] *United States Naval Academy, Annapolis, MD 21402, USA*
[47] *Valparaiso University, Valparaiso, Indiana 46383, USA*
[48] *Variable Energy Cyclotron Centre, Kolkata 700064, India*
[49] *Warsaw University of Technology, Warsaw, Poland*
[50] *University of Washington, Seattle, Washington 98195, USA*
[51] *Wayne State University, Detroit, Michigan 48201, USA*
[52] *Yale University, New Haven, Connecticut 06520, USA*
[53] *University of Zagreb, Zagreb, HR-10002, Croatia*

We report measurements of the charge-separated $W^{+(-)} \to e^{+(-)} + \nu_e(\bar{\nu}_e)$ and $Z/\gamma^* \to e^+e^-$ production cross sections at mid-rapidity in proton-proton collisions at $\sqrt{s} = 500$ GeV. These results are based on 13.2 pb^{-1} of data recorded in 2009 by the STAR detector at RHIC. Production cross sections for W bosons that decay via the $e\nu$ channel were measured to be $\sigma(pp \to W^+X)\cdot\mathrm{BR}(W^+ \to e^+\,\nu_e) = 117.3 \pm 5.9(\mathrm{stat}) \pm 6.2(\mathrm{syst}) \pm 15.2(\mathrm{lumi})$ pb, and $\sigma(pp \to W^-X)\cdot\mathrm{BR}(W^- \to e^-\,\bar{\nu}_e) = 43.3 \pm 4.6(\mathrm{stat}) \pm 3.4(\mathrm{syst}) \pm 5.6(\mathrm{lumi})$ pb. For Z/γ^* production, $\sigma(pp \to Z/\gamma^*X)\cdot\mathrm{BR}(Z/\gamma^* \to e^+e^-) = 7.7 \pm 2.1(\mathrm{stat})\,^{+0.5}_{-0.9}(\mathrm{syst}) \pm 1.0(\mathrm{lumi})$ pb was measured for di-lepton invariant masses $m_{e^+e^-}$ between 70 and 110 GeV/c^2. First measurements of the W cross section ratio, $\sigma(pp \to W^+X)/\sigma(pp \to W^-X)$, at $\sqrt{s} = 500$ GeV are also reported. Theoretical predictions, calculated using recent parton distribution functions, are found to agree with the measured cross sections.

PACS numbers: 14.20.Dh, 13.38.Be, 13.85.Qk, 14.70.Fm

I. INTRODUCTION

Studies of inclusive W and Z/γ^* boson production in proton-proton collisions provide valuable information, both to test the Standard Model of particle physics and to advance our understanding of the proton's substructure. Measurements of the production cross sections $\sigma(pp \to W^{+(-)}X) \cdot \mathrm{BR}(W^{+(-)} \to e^{+(-)} + \nu_e(\bar{\nu}_e))$ and $\sigma(pp \to Z/\gamma^* X) \cdot \mathrm{BR}(Z/\gamma^* \to e^+e^-)$ can be compared to theoretical calculations that involve the weak couplings between intermediate vector bosons and quarks, and which must account for higher-order terms in perturbative QCD. Such calculations also rely on models of the parton distribution functions (PDFs) for the quarks and, in pp collisions, for the antiquark 'sea.'

Until recently, most measurements of W and Z/γ^* production in hadronic interactions have been confined to experiments using proton-antiproton collisions. First results were obtained by the UA1 [1, 2] and UA2 [3, 4] collaborations at $\sqrt{s} = 630$ GeV at the CERN Sp$\bar{\mathrm{p}}$S facility, followed by the CDF [5, 6] and D0 [7, 8] $p\bar{p}$ measurements at the Fermilab Tevatron, at $\sqrt{s} = 1.8$ and 1.96 TeV. It is only in the last few years that pp colliders have reached sufficient center of mass energies for comparable studies, at $\sqrt{s} = 500$ GeV by the STAR (Solenoidal Tracker at RHIC) [9] and PHENIX [10] collaborations at the Relativistic Heavy Ion Collider (RHIC), and most recently by the LHC experiments ATLAS [11] and CMS [12, 13] at $\sqrt{s} = 7$ TeV.

RHIC is unique in its capability to collide high energy polarized proton beams, and the observation of W production in these polarized proton collisions provides a new means to explore the spin-flavor structure of proton sea quark distributions. First measurements of the parity-violating longitudinal single-spin asymmetry for $W^{\pm}$ decay leptons have also been reported by the STAR [9] and PHENIX [10] collaborations and are in good agreement with predictions from NLO and resummed calculations [14, 15].

At hadron colliders, the leading process in $W^{+(-)}$ production is $u + \bar{d}\,(d + \bar{u})$ fusion. This suggests that while the W^+ and W^- production cross sections should be close to equal in $p\bar{p}$ collisions, they can be expected to differ in pp measurements due to differences in the u and d quark and antiquark distributions within the proton. The PDFs that characterize the valence u and d quarks of the proton (or $\bar{u}$ and $\bar{d}$ in the antiproton) are well determined from decades of high precision, deep-inelastic lepton scattering experiments (see, for example, Ref. [16]). Comparable distributions for the antiquarks within the proton sea, however, are much more weakly constrained. Interest in these poorly-known antiquark PDF's has also increased over the last few years, due to results from Drell-Yan experiments [17, 18] which find evidence for a much larger $\bar{d}/\bar{u}$ flavor asymmetry in the nucleon than had been anticipated, especially at momentum fractions near and above $x \sim 0.2$. Detailed measurements of $W^{\pm}$ and Z/γ^* production in proton-proton collisions will provide new and complementary information about this flavor asymmetry in the sea, from different reactions and at very different momentum scales.

This paper describes the first measurement of the W^+, W^-, and Z/γ^* boson production cross sections in proton-proton collisions at $\sqrt{s} = 500$ GeV by the STAR collaboration at RHIC. The cross sections are derived from studies of the charge-separated $W^{+(-)} \to e^{+(-)} + \nu_e(\bar{\nu}_e)$ and $Z/\gamma^* \to e^+e^-$ decay channels for outgoing leptons near mid-rapidity ($|\eta_e| < 1$), and are based on 13.2 pb^{-1} of data recorded during the 2009 run. In addition to the individual cross sections, a first measurement of the W^+/W^- cross section ratio at $\sqrt{s} = 500$ GeV is also presented.

The paper is organized as follows. Section II provides a brief overview of the STAR detector, focusing on the subsystems used in this analysis. Section III describes the data and simulation samples analyzed, Sec. IV details the extraction of the W and Z/γ^* signal spectra, and Sec. V explains the estimation and subtraction of the background from the signal spectra. Finally, we discuss the calculation of the W and Z/γ^* production cross sections in Sec. VI and the W^+/W^- cross section ratio in Sec. VII, and compare these results to several theoretical calculations. Some of the data analysis methods employed here have been described briefly in Ref. [9], and are discussed in more detail in this paper which incorporates a slightly larger data sample as well as improved detector calibrations.

II. THE STAR DETECTOR

The STAR detector [19], shown schematically in Fig. 1, is a large acceptance, multipurpose detector designed primarily for measurements of hadronic and electromagnetic particle production in high-energy heavy ion and polarized proton-proton collisions. STAR is comprised of many separate subsystems, each with specific capabilities; only those subsystems most relevant for the present analysis will be mentioned below.

The heart of STAR is a large Time Projection Chamber (TPC) [20] which is situated within a highly uniform, 0.5 T solenoidal magnetic field. The TPC provides charged particle tracking, particle identification (via ionization energy loss, dE/dx), and precision momentum measurements over the range $|\eta| < 1.3$ and with full 2π azimuthal coverage. Although the p_T resolution of the TPC deteriorates with increasing p_T, the spacial accuracy of tracks reconstructed between the inner and outer radius of the TPC, located at 50 and 200 cm respectively, remains accurate up to ∼1-2 mm in Cartesian

space. In this analysis, TPC tracks were used in identifying the high-p_T $e^{\pm}$ candidates, determining candidate charge signs, reducing contamination from the significant QCD background (see Sec. IV), and reconstructing the pp interaction vertex for the events of interest.

Surrounding the TPC radially is the Barrel Electromagnetic Calorimeter (BEMC) [21], a high granularity lead/scintillator-based sampling calorimeter. This detector is used to measure the energy deposited by energetic photons and electrons with pseudorapidities $|\eta| < 1.0$ over the full azimuth. The BEMC is segmented into 4800 optically isolated projective towers, each of which subtends 0.05 rad in azimuth (ϕ) and 0.05 units in η, and is roughly 20 radiation lengths deep. Based on cosmic ray and test beam data, the nominal energy resolution of the barrel calorimeter is calculated to be $\delta E/E = 14\%/\sqrt{E(\mathrm{GeV})} \oplus 1.5\%$ [21]. The BEMC was used to measure the $e^{\pm}$ candidate energy, and to aid in background reduction. By identifying events with large, highly localized, electromagnetic energy deposition, the BEMC also provided our first-level trigger signal for leptonic W and Z decays.

Located at one end of the STAR TPC, directly in front of the magnetic field return poletip, is the Endcap Electromagnetic Calorimeter (EEMC) [22], which provides electromagnetic energy measurement over the range $1.09 < \eta < 2$ and 2π in azimuth. The EEMC is similar in design to the BEMC: a lead/scintillator sampling calorimeter, finely segmented in η and ϕ into 720 towers with projective geometries, though it is approximately 3-4 radiation lengths thicker than the BEMC due to its more forward position. In the work presented here, the EEMC was only used for background reduction, via the isolation and missing energy requirements discussed in Sec. IV.

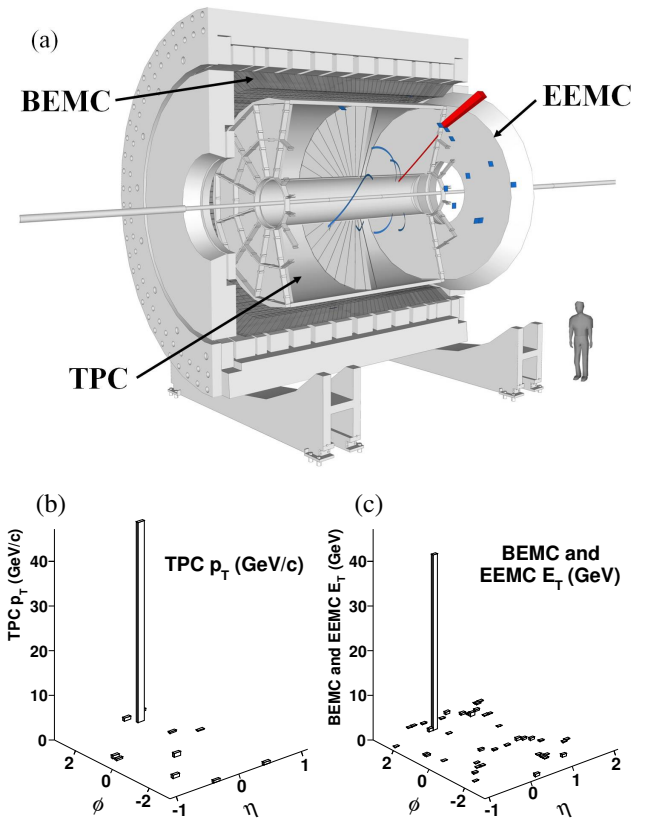

FIG. 1. (Color online) (a) W candidate event display embedded in a schematic of the STAR detector. Descriptions of the subsystems relevant for this analysis are given in Sec. II. (b) TPC p_T and (c) BEMC and EEMC E_T distributions in η and ϕ for the same W candidate event as shown in (a).

III. DATA AND SIMULATION SAMPLES

Events in this analysis were selected online using a two-level trigger requirement in the BEMC. The hardware level-0 trigger accepted events containing at least one tower with a transverse energy, E_T, greater than 7.3 GeV. A dedicated software trigger algorithm then selected events by constructing 2×2 clusters of towers, and requiring that at least one cluster consist of a seed tower with $E_T > 5$ GeV and a cluster sum $E_T > 13$ GeV. During the 2009 run 1.2×10^6 events were recorded satisfying these trigger conditions.

A. Luminosity Measurement

The integrated luminosity of the data sample was determined using the Vernier Scan technique [23]. The transverse widths (σ_x and σ_y) of the beam overlap region are determined by measuring the trigger rate as the beams are swept through each other in the transverse plane. The intensity of each beam is determined during a scan by the Wall Current Monitors (WCM) [24]. With the assumption of Gaussian beams, the instantaneous luminosity can be written as

$$\mathcal{L} = \frac{f_{rev} K}{2\pi\sigma_x\sigma_y} \quad (1)$$

where f_{rev} is the revolution frequency and $K = \sum N_i^a N_i^b$ is the product of the bunch intensities (N_i) of the two beams (a,b) summed over all bunches. The dedicated trigger used in the Vernier Scan, and also to monitor the luminosity in this analysis, is the level-0 hardware trigger, described above, with a coincidence away-side E_T requirement imposed offline to reduce non-collision background. The cross section for this trigger can be written as $\sigma_{\mathrm{ver}} = \mathrm{R}_{\mathrm{ver}}^{\mathrm{max}}/\mathcal{L}$, where $\mathrm{R}_{\mathrm{ver}}^{\mathrm{max}}$ is the maximum trigger rate while the beams are fully overlapping. The value measured for this work was $\sigma_{\mathrm{ver}} = 434 \pm 8(\mathrm{stat}) \pm 56(\mathrm{syst})$ nb. Figure 2 shows an example of the trigger rate as a function of the x and y beam displacements during one of the vernier scans, which was fit to extract the transverse beam widths and maximum trigger rate. The fit function used was a Gaussian in x and y combined with

a constant term to account for remaining non-collision background. The largest contribution to the $\sigma_{\rm ver}$ systematic uncertainty was attributed to possible non-Gaussian components of the beam profile (10%), with smaller contributions coming from possible BEMC gain drift (5%), and uncertainties in the bunch intensity measurements (4%). This value for $\sigma_{\rm ver}$ was used to normalize the total number of events which satisfy this trigger condition, resulting in an integrated luminosity for the data sample of $L = \int \mathcal{L}\, dt = 13.2 \pm 0.2(\text{stat}) \pm 1.7(\text{syst})$ pb^{-1}.

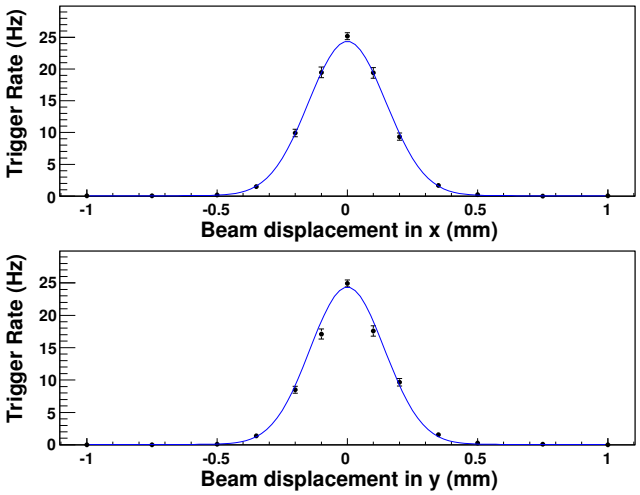

FIG. 2. (Color online) Trigger rate as a function of vernier scan beam displacement in the x and y directions. The transverse beam widths (σ_x and σ_y) and maximum trigger rate ($\mathrm{R}_{\rm ver}^{\rm max}$) were extracted from the fit, which is superimposed.

B. Simulation Samples

Monte-Carlo (MC) simulation samples were generated in order to determine detector efficiencies, estimate background contributions from electroweak processes, and compare various predicted observables to data. Signal samples for both the $W \to e\nu$ and $Z/\gamma^* \to e^+e^-$ channels were generated, along with a $W \to \tau\nu$ sample which is an expected background in the W analysis due to the τ's leptonic decay. All the samples were produced using the PYTHIA 6.422 [25] event generator and a GEANT [26] model of the STAR detector response. The same reconstruction and analysis algorithm was used for both the data and MC samples, and each MC sample was normalized to the integrated luminosity of the data unless otherwise stated.

Due to the high luminosity of the pp collision environment at $\sqrt{s} = 500$ GeV at STAR, a significant number of pile-up tracks are present in the TPC at any given time. The pile-up tracks are the result of either another collision from the same bunch crossing as the triggered event, or a collision that occurred in an earlier or later bunch crossing. Note that the bunch crossing period at RHIC is about 107 ns, while it can take up to $\sim$38 μs for track ionization to drift through the TPC. In the simulation, these pile-up tracks are accounted for by embedding the full GEANT detector response of the simulated event into a zero-bias triggered event before reconstruction. The zero-bias events are selected randomly during nominal beam crossings at a rate of $\lesssim$ 1Hz with no detector requirements, resulting in a good representation of the pile-up contained in the TPC for BEMC triggered collision events.

IV. W AND Z/γ^* SIGNAL RECONSTRUCTION

This section details the identification and reconstruction of W and Z/γ^* candidate events, as well as the reduction of the large QCD background. This reduction is achieved through cuts designed to take advantage of the kinematical and topological differences between electroweak and QCD processes. "Z/γ^*" will be used interchangeably with "Z" for the remainder of this paper.

Candidate events were selected from the sample of BEMC triggered events described in Sec. III by requiring a reconstructed primary vertex. A primary vertex is one reconstructed from either a single TPC track with $p_T > 10$ GeV/c or multiple tracks originating from the same location along the beamline. Each track considered in vertex reconstruction is assigned an increased weight if it either points to a region of energy deposition in the calorimeters, or if it uses hit points from both sides of the TPC central membrane. Tracks satisfying either of these two conditions are likely to be from the triggered collision, therefore weighting these tracks more heavily in vertex reconstruction strongly reduces the contamination from pile-up tracks. The distribution of primary vertices along the beam direction is approximately Gaussian with an RMS width of 52 cm. Events of interest were required to have a $|z_{\rm vertex}| < 100$ cm, where $z_{\rm vertex}$ is the distance along the beam direction of the primary vertex from the center of the STAR interaction region.

A. Identification of High-E_T Isolated Electrons and Positrons

A candidate electron or positron track is defined to be a TPC track with $p_T > 10$ GeV/c that is associated with a primary vertex satisfying the criteria described above. Candidate tracks were also required to have:

- a minimum of 15 TPC points,
- more than 51% of the maximum number of TPC points allowed,
- a first TPC point with radius less than 90 cm,
- a last TPC point with radius greater than 160 cm.

These requirements help to ensure that the track and its charge sign are well reconstructed, as well as reject

pile-up tracks which may be mistakenly associated with a primary vertex. Candidate TPC tracks are extrapolated to the BEMC to determine to which tower the track points, then the four possible 2×2 BEMC tower clusters containing the tower pointed to by the track are formed. The 2×2 cluster with the largest summed transverse energy, E_T^e, is assigned to the $e^{\pm}$ candidate. The E_T^e is required to be greater than 15 GeV to be safely above the trigger turn-on region. Also, the two dimensional distance between the energy log-weighted centroid of the tower cluster position and the extrapolated TPC track position, $|\Delta\vec{r}|$, is required to be less than 7 cm, to reject candidates where the BEMC cluster may not have originated from the particle which produced the high p_T TPC track.

Electrons and positrons from W and Z decays should be well isolated from other particles in $\eta - \phi$ space; thus, in the next stage of the candidate selection process two isolation criteria are applied. The first isolation cut was made by summing the E_T in the 4×4 BEMC tower cluster which surrounds the $e^{\pm}$ candidate cluster, $E_T^{4\times4}$, and requiring $E_T^e/E_T^{4\times4} > 0.95$. The other isolation requirement is imposed to reduce jet-like events. The quantity $E_T^{\Delta\mathrm{R}<0.7}$ is defined as the sum of all BEMC and EEMC tower E_T and TPC track p_T within a cone radius of $\Delta\mathrm{R} = \sqrt{\Delta\eta^2 + \Delta\phi^2} < 0.7$ around the candidate track, and the ratio $E_T^e/E_T^{\Delta\mathrm{R}<0.7}$ is required to be greater than 0.88. The $e^{\pm}$ candidate track is excluded from the sum of TPC track p_T to avoid double-counting the candidate energy in the $E_T^{\Delta\mathrm{R}<0.7}$ sum. Figure 3 shows the isolation ratios described above for both data and $W \to e\nu$ MC. The values of the cuts, shown by the dashed lines, were chosen to retain a large fraction of the signal, while significantly reducing the QCD background. Note that differences between the isolation ratios in Fig. 3 of this paper and Fig. 1 of Ref. [9] are expected due to differences in the data samples used and improved calibrations. Also, the order of the $E_T^e/E_T^{4\times4}$ and candidate track-cluster matching $|\Delta\vec{r}|$ cuts were inverted in Ref. [9] with respect to the ordering described in this section.

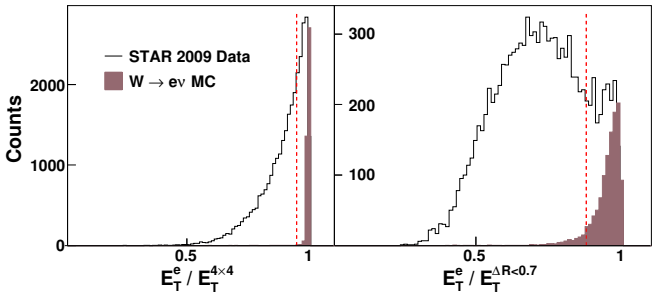

FIG. 3. (Color online) Distributions of the isolation ratios $E_T^e/E_T^{4\times4}$ (left) and $E_T^e/E_T^{\Delta\mathrm{R}<0.7}$ (right) used in $e^{\pm}$ candidate selection. $W \to e\nu$ MC shape distributions (arbitrary normalization) are shown as filled histograms for comparison with the data distributions. The vertical dashed lines indicate the values of the cuts on these isolation ratios.

B. *W* Candidate Event Selection

The selection of $W \to e\nu$ candidate events is based on differences in the event topology between leptonic W decays and the QCD background or $Z \to e^+e^-$ events. $W \to e\nu$ events contain a nearly isolated $e^{\pm}$ with a neutrino close to opposite in azimuth. Electrons and positrons emitted near mid-rapidity from W decay are characterized by a large E_T^e that peaks near half the W mass (∼40 GeV) with a distribution referred to as a Jacobian peak. There is also a large missing transverse energy in $W \to e\nu$ events opposite, in azimuth, to the $e^{\pm}$ due to the undetected neutrino. As a result, there is a large imbalance in the vector p_T sum of all reconstructed final state objects for W events. In contrast, $Z \to e^+e^-$ events and QCD hard-scattering events, such as di-jets, are characterized by a small magnitude of this vector p_T sum imbalance.

In order to enforce this missing transverse energy requirement, we define the p_T balance vector:

$$\vec{p}_T^{\,bal} = \vec{p}_T^{\,e} + \sum_{\Delta\mathrm{R}>0.7} \vec{p}_T^{\,jets} \qquad (2)$$

where $\vec{p}_T^{\,e}$ is the $e^{\pm}$ candidate p_T vector, which is composed of a momentum direction and a magnitude determined by the candidate TPC track and BEMC cluster, respectively. The second term on the right of Eq. 2 is the sum of the p_T vectors for all reconstructed jets whose thrust axes are *outside* the cone radius of $\Delta\mathrm{R} = 0.7$ around the $e^{\pm}$ candidate. Jets are reconstructed using a standard mid-point cone algorithm used in STAR jet measurements [27] based on the tracks from the TPC and tower energies in the BEMC and EEMC. A scalar signed P_T-balance variable is then formed, defined as

$$\text{signed } P_T\text{-balance} = \mathrm{sign}\left(\vec{p}_T^{\,e} \cdot \vec{p}_T^{\,bal}\right) \left|\vec{p}_T^{\,bal}\right|. \qquad (3)$$

This quantity is required to be larger than 15 GeV/c as indicated by the dashed line in Fig. 4. Also in Fig. 4 one can see that in the $W \to e\nu$ MC sample, the signed P_T-balance variable and E_T^e are very well correlated, as contributions to the $\vec{p}_T^{\,bal}$ vector from reconstructed jets outside the cone of $\Delta\mathrm{R} = 0.7$ are generally small. The data show a similar correlation at high E_T^e, where the distribution is dominated by $W \to e\nu$ events. At low E_T^e where contributions from QCD background events are larger, more events have a small value for the signed P_T-balance variable, as expected.

The signed P_T-balance requirement provides a significant suppression of QCD di-jet and $Z \to e^+e^-$ background events, and a further reduction of the $Z \to e^+e^-$ background is achieved by rejecting events with an additional e-like 2×2 cluster in a reconstructed jet where $E_T^{2\times2} > p_T^{jet}/2$ and the invariant mass of the two $e^{\pm}$-like clusters is within the range of 70 to 140 GeV/c^2. This reduces $Z \to e^+e^-$ contamination in both the W signal sample and in the sample that will be used for the data-driven QCD background, described in Sec. V A.

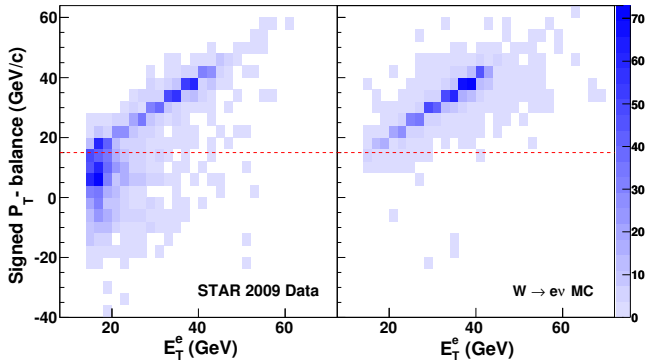

FIG. 4. (Color online) Correlation of the signed P_T-balance variable and E_T^e for data (left) and $W \to e\nu$ MC (right).

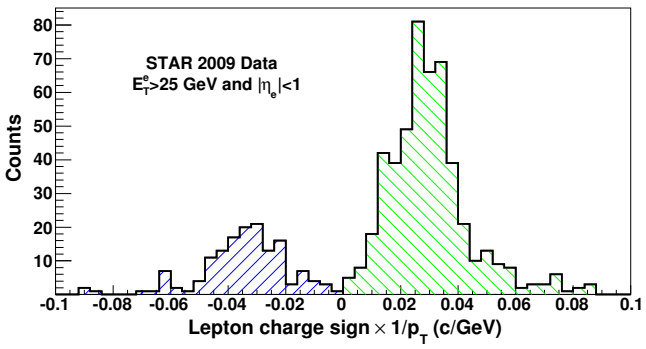

FIG. 6. (Color online) Distribution of the product of the TPC reconstructed charge sign and $1/p_T$ for candidates satisfying all the W signal selection criteria and $E_T^e > 25$ GeV.

The reduction in the W candidate yield after each of the selection criteria is shown in Fig. 5. Initially, when only a candidate TPC track and BEMC cluster have been reconstructed, the distribution (solid line) is dominated by QCD background, which is exponentially falling with E_T^e, and there is no evidence of the Jacobian peak. However, once the $e^{\pm}$ selection, isolation and signed P_T-balance cuts are applied, a W signal can be seen above the background at $E_T^e \sim M_W/2$.

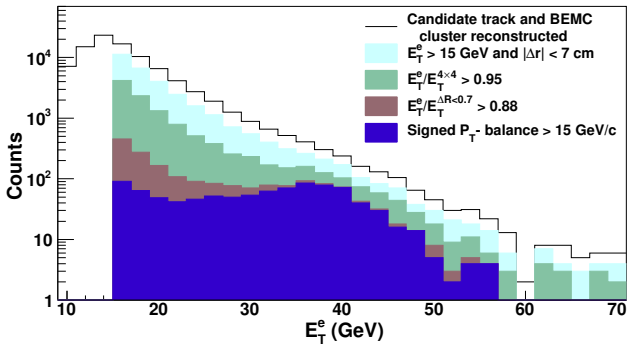

FIG. 5. (Color online) Distributions of E_T^e for W candidate events after sequentially applying the selection criteria described in Secs. IV A and IV B.

The charge sign of the $e^{\pm}$ candidate is determined by the direction of curvature of the TPC track in the STAR magnetic field, while the magnitude of the track curvature provides a measure of $1/p_T$. Figure 6 shows the product of the reconstructed charge sign and $1/p_T$ for the lepton candidates that satisfy all the cuts described above with $E_T^e > 25$ GeV. Two well-separated regions are seen for the positive and negative charges, cleanly distinguishing between the e^+ and e^- candidates.

C. Z Candidate Event Selection

Using the isolated $e^{\pm}$ sample found in Sec. IV A, $Z \to e^+e^-$ events were selected by requiring a pair of isolated $e^{\pm}$ candidates with opposite charge signs. The invariant mass of each e^+e^- pair was reconstructed, and the resulting mass distributions are shown in Fig. 7 after each of the selection criteria described in Sec. IV A has been satisfied for both the e^+ and e^- candidates. After

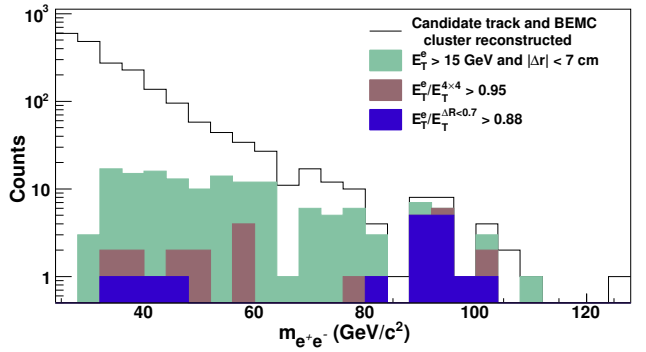

FIG. 7. (Color online) Distributions of the invariant mass of pairs of oppositely charged $e^{\pm}$ candidates after sequentially applying the selection criteria described in Sec. IV A to both $e^{\pm}$ candidates.

all selection cuts are applied, there is a signal near the invariant mass of the Z and a small signal at lower invariant mass. This is consistent with the expectations from the $Z/\gamma^* \to e^+e^-$ MC, as shown in Fig. 8.

V. BACKGROUND ESTIMATION

A. W Background Estimation

There are a number of background processes that can contribute to the $W \to e\nu$ candidate yield. Other electroweak processes yield isolated electrons as well, which can be misidentified as $W \to e\nu$ events. Also, QCD jets may fragment in such a way that they satisfy the isolated electron requirements, and detector acceptance effects can allow these events to satisfy the remaining

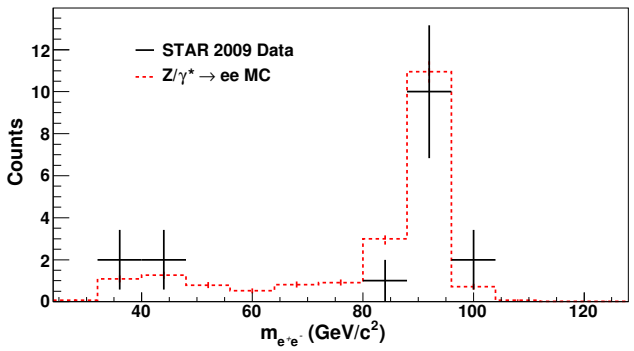

FIG. 8. (Color online) Distributions of the invariant mass of $Z/\gamma^* \to e^+e^-$ candidate events satisfying all selection criteria described in Sec. IV C. The $Z/\gamma^* \to e^+e^-$ MC distribution (dashed line) is shown for comparison. Note the larger bin widths relative to Fig. 7

$W \to e\nu$ event selection criteria. This section describes how the contributions of these background processes are estimated.

The electroweak background processes considered in this analysis are $W \to \tau\nu$ and $Z \to e^+e^-$. Their contributions to the $W \to e\nu$ signal yield were estimated using the MC samples described in Sec. III B. $W \to \tau\nu$ events, where the τ decays leptonically (*i.e.* $\tau \to e\nu\bar{\nu}$), contain an isolated $e^\pm$ with a large missing energy opposite in azimuth, similar to the $W \to e\nu$ signal. However, the $e^\pm$ which comes from the τ decay must share the energy of the τ with the two secondary neutrinos, and thus it has a much lower E_T^e on average than those $e^\pm$ which come directly from a W decay. Therefore, the $W \to \tau\nu$ background contributions are largest at low E_T^e, as can be seen in Fig. 9. $Z \to e^+e^-$ events can contaminate the W signal when one of the decay leptons escapes detection, either from a detector inefficiency or by traversing an uninstrumented region of phase space. Unlike the other background sources described in this section, the $Z \to e^+e^-$ background yield is approximately constant in E_T^e, resulting in a significant contribution to the total background, even though the cross section is small compared to other processes. Table I lists each of the background processes and its estimated contribution to the W yield for candidates with $E_T^e > 25$ GeV. The uncertainties for these electroweak background components are due to the statistical uncertainty of the MC calculation and the uncertainty in the normalization of the MC samples to the integrated luminosity of the data.

The STAR detector has only one EEMC, resulting in missing calorimetry acceptance for the pseudorapidity region $-2 < \eta < -1.09$ compared to the positive pseudorapidity portion of the detector. If the isolation cone of $\Delta R < 0.7$ around an $e^\pm$ candidate overlaps with this missing acceptance, or a jet opposite in azimuth of an $e^\pm$ candidate falls within this acceptance, background QCD events may satisfy all the $W \to e\nu$ selection requirements. This contamination of the W yield, referred to as the 'second EEMC' background, was determined by repeating the W signal selection a second time, with the EEMC towers excluded from the isolation ratio, $E_T^e/E_T^{\Delta R<0.7}$, and the reconstruction of jets summed in the $\vec{p}_T^{\,bal}$ vector. The events which satisfy the requirements of this second pass analysis (without the EEMC), but fail the nominal requirements described in Secs. IV A and IV B are a direct measure of the background rejected by the EEMC. Moreover, these events also estimate the amount of background that would have been rejected by a second EEMC.

While this sample of second EEMC background is expected to be predominantly the result of QCD processes, it does contain a small amount of $Z \to e^+e^-$ contamination as well. Because background from the $Z \to e^+e^-$ process was already taken into account separately, the $Z \to e^+e^-$ MC sample was used to remove any contamination from $Z \to e^+e^-$ processes in the second EEMC background distribution, to avoid double-counting. The uncertainty on the second EEMC background is the statistical uncertainty of the events vetoed by the EEMC and the systematic uncertainty in the normalization of $Z \to e^+e^-$ contamination which was subtracted using the $Z \to e^+e^-$ MC.

The remaining contribution to the background is predominantly from QCD $2 \to 2$ processes in which one jet fragments such that it satisfies our $e^\pm$ candidate requirements, while all other jets escape detection outside the $|\eta| < 2$ acceptance. This component of the background was estimated using a data-driven QCD background distribution as a function of E_T^e, which is obtained by selecting events which satisfy all the isolated $e^\pm$ candidate criteria, but have a signed P_T-balance < 15 GeV/c. Similar to the way the second EEMC background was corrected, contributions to the data-driven background distribution from the $Z \to e^+e^-$ process were removed using the $Z \to e^+e^-$ MC sample, to avoid double-counting the $Z \to e^+e^-$ background.

The data-driven QCD background distribution was then normalized to the remaining $W \to e\nu$ candidate signal distribution after the $W \to \tau\nu$, $Z \to e^+e^-$, and second EEMC background components had been removed. The normalization was determined over the range $15 < E_T^e < 19$ GeV, and accounts for the possibility of true W signal events in this region using the $W \to e\nu$ MC. The systematic uncertainty of this data-driven QCD background contribution was estimated by varying the data-driven background distribution and the E_T^e region over which the distribution was normalized. Twenty different background distributions were obtained by varying the cut on the signed P_T-balance variable from 5 to 25 GeV/c in steps of 1 GeV/c. The twenty background distributions were then fit to the signal, as described above, using three different normalization regions ($15 < E_T^e < 17$, 19, and 21 GeV), resulting in sixty different normalized background distributions. The systematic uncertainty in each E_T^e bin was taken to be the largest deviation among these sixty distributions from

the nominal value.

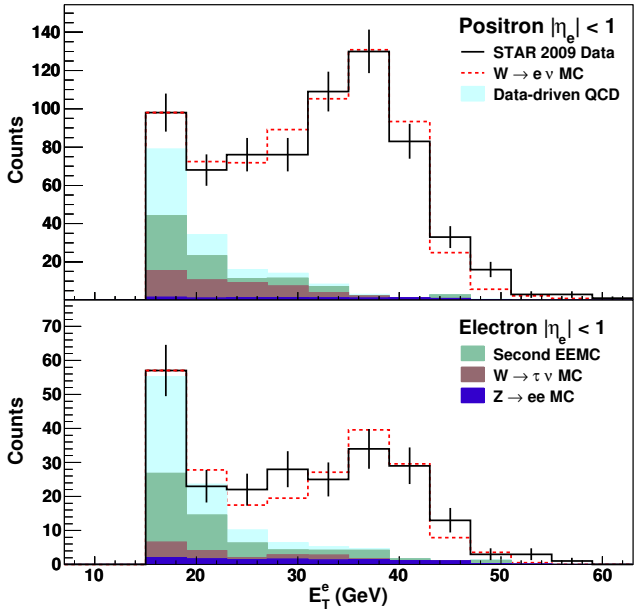

FIG. 9. (Color online) E_T^e distribution of W^+ (top) and W^- (bottom) candidate events, background components, and $W \to e\nu$ MC signal for comparison. Note the factor of two difference in the vertical scales.

	$W^+ \to e^+ \nu_e$	$W^- \to e^- \bar{\nu}_e$
$W \to \tau\nu$	$13.4 \pm 1.7 \pm 3.2$	$3.3 \pm 0.8 \pm 0.8$
$Z \to e^+e^-$	$7.3 \pm 0.4 \pm 1.7$	$7.3 \pm 0.4 \pm 1.7$
Second EEMC	$9.1 \pm 3.0 \pm 0.5$	$9.2 \pm 3.0 \pm 0.4$
Data-driven QCD	$7.0 \pm 0.6\ ^{+2.3}_{-1.6}$	$5.8 \pm 0.5\ ^{+2.6}_{-1.2}$
Total	$36.6 \pm 3.5\ ^{+5.4}_{-5.2}$	$25.8 \pm 3.2\ ^{+3.6}_{-2.8}$

TABLE I. Summary of background event contributions to the $W \to e\nu$ yield and their uncertainties for candidates with $E_T^e > 25$ GeV and $|\eta_e| < 1$.

The charge-separated E_T^e distributions of $W^\pm \to e^\pm + \nu_e$ candidates satisfying all the selection criteria described in Secs. IV A and IV B are shown in Fig. 9. Also shown here are the contributions from the different backgrounds discussed in this section and the $W \to e\nu$ signal MC distribution, which is normalized to the integrated luminosity of the data. A χ^2 test of homogeneity comparing the data and the sum of background components and $W \to e\nu$ signal MC (dashed line) E_T^e spectra results in a χ^2 value of 9.5 and 6.9 for the W^+ and W^-, respectively. For 12 degrees of freedom this results in a 66% and 86% probability, respectively, to obtain a larger χ^2. This indicates a good agreement between data and MC and further validates the procedure used in the background estimation described in this section. The $e^\pm$ pseudorapidity distributions are shown in Fig. 10, where the background contributions were found independently for each η_e bin using the methods described above. Again, good agreement is found between the data and the sum of the $W \to e\nu$ signal MC and background components.

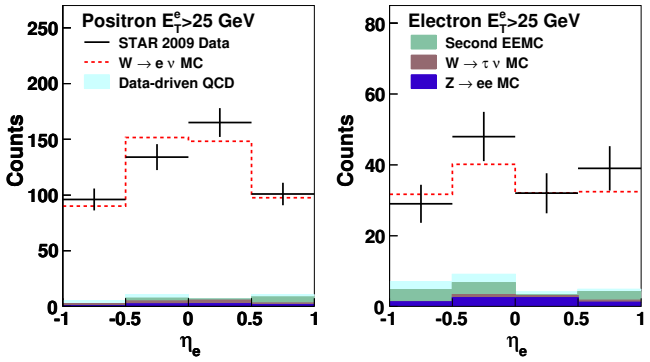

FIG. 10. (Color online) Lepton pseudorapidity distribution of W^+ (left) and W^- (right) candidate events, background components, and $W \to e\nu$ MC signal for comparison.

B. Z Background Estimation

The background for the $Z \to e^+e^-$ signal is expected to be very small due to the coincidence requirement of a pair of oppositely charged, high E_T, isolated e^+ and e^-. Background contributions from electroweak processes were estimated using the MC samples described in Sec. III B. Within the defined mass window to be used for the cross section measurement ($70 < m_{e^+e^-} < 110$ GeV/c^2), the background contributions were determined to be $0.1\ ^{+0.3}_{-0.1}$ events from $W \to e\nu$ and negligible from the other Z decay channels. The $W \to e\nu$ background uncertainty was estimated using the 68% C.L. interval of the unified statistical approach described in Ref. [28].

An accurate data-driven estimate of the QCD background is difficult to obtain for the Z signal due to the limited statistics of the data set. One method for estimating the background is to determine the number of $e^\pm$ pairs that satisfy all the $Z \to e^+e^-$ signal criteria other than the opposite charge-sign requirement. However, no same charge-sign pairs were observed in the data, therefore, the QCD background was found to be consistent with zero. An upper bound on the QCD background systematic uncertainty was estimated to be 1.3 events using a 68% C.L. interval [28].

VI. THE W AND Z CROSS SECTIONS

The W and Z production cross sections were measured from the sample of events which satisfy the fiducial and kinematic requirements of this analysis. As stated previously, only $e^\pm$ candidates at mid-rapidity ($|\eta_e| < 1$) were considered in this analysis. Candidates for the W analysis must have $E_T^e > 25$ GeV, and for the Z analysis we

required that both e^+ and e^- have $E_T^e > 15$ GeV and $70 < m_{e^+e^-} < 110$ GeV/c^2. The cross sections measured within these constraints are defined as the fiducial cross sections, and can be written as:

$$\sigma^{fid}_{W(Z)} \cdot \mathrm{BR}(W(Z) \to e\nu(ee)) = \frac{N^{obs}_{W(Z)} - N^{bkgd}_{W(Z)}}{L \cdot \epsilon^{tot}_{W(Z)}} \quad (4)$$

where

- $N^{obs}_{W(Z)}$ is the number of observed $W(Z)$ candidates within the defined kinematic acceptance satisfying all the selection criteria described in Sec. IV,
- $N^{bkgd}_{W(Z)}$ is the total number of $W(Z)$ background events within the defined kinematic acceptance satisfying all the selection criteria described in Sec. IV, and estimated from various contributions described in Sec. V,
- $\epsilon^{tot}_{W(Z)}$ is the total efficiency correction described in Sec. VI A below,
- and L is the integrated luminosity of the data set discussed in Sec. III A.

To determine the total production cross sections, it is necessary to apply acceptance correction factors, $A_{W(Z)}$, to the fiducial cross sections defined above, to account for the fiducial and kinematic constraints imposed in the analysis. The total production cross sections are then defined via the relations

$$\sigma^{tot}_W \cdot \mathrm{BR}(W \to e\nu) = \frac{\sigma^{fid}_W \cdot \mathrm{BR}(W \to e\nu)}{A_W} \quad (5)$$

$$\sigma^{tot}_Z \cdot \mathrm{BR}(Z \to e^+e^-) = \frac{\sigma^{fid}_Z \cdot \mathrm{BR}(Z \to e^+e^-)}{A_Z}. \quad (6)$$

The determination of the acceptance corrections necessary to extract the total production cross sections is discussed in Sec. VI C.

A. The Efficiency Correction Factors

The efficiency corrections were obtained using the $W \to e\nu$ and $Z \to e^+e^-$ PYTHIA MC samples described in Sec. III B. Only the subset of events from the MC samples which satisfy the acceptance conditions for the fiducial cross sections were used in the efficiency calculations, as the acceptance correction is accounted for separately in the definition of the total cross section.

The total efficiency can be factorized into four efficiency terms, written as:

$$\epsilon^{tot}_{W(Z)} = \epsilon^{trig}_{W(Z)} \cdot \epsilon^{vert}_{W(Z)} \cdot \epsilon^{trk}_{W(Z)} \cdot \epsilon^{algo}_{W(Z)}. \quad (7)$$

The values for each of the terms in Eq. 7 are listed in Table II, along with their uncertainties, for the W^+, W^-, and Z signals. The remainder of this section describes how those values were obtained.

The trigger efficiency, ϵ^{trig}, is the fraction of MC signal events which satisfy the online trigger condition defined in Sec. III. This was determined by emulating the trigger condition used online in the MC. Due to the relatively wide z_{vertex} distribution of our data sample, some candidates may satisfy the $|\eta_e| < 1$ kinematic condition at the MC generator level, but will fall outside the acceptance of the BEMC. This was observed in the W analysis as an E_T^e-dependent trigger efficiency due to the correlation of the E_T^e and η_e of the decay $e^\pm$. An E_T^e-dependent trigger efficiency correction was therefore used in the computation of the $W^\pm$ cross sections. This effect also leads to a notably smaller average W^- trigger efficiency relative to W^+, as the η_e distribution is expected to be peaked more strongly at zero for the W^+ candidates than W^-, which is consistent with Fig. 10. To estimate the uncertainty on ϵ^{trig}, the BEMC energy scale was varied by its uncertainty of $\pm 3.6\%$. Because the offline kinematic requirement of $E_T^e > 25$ GeV was significantly larger than the trigger threshold of 13 GeV, for this analysis we observed only small variations in the trigger efficiency due to the uncertainty of the BEMC energy calibration.

The vertex efficiency, ϵ^{vert}, is defined as the fraction of events satisfying the trigger which contain a reconstructed primary vertex within the fiducial cut of $|z_{\mathrm{vertex}}| < 100$ cm, as described in Sec. IV. The tracking efficiencies for the W and Z decay $e^\pm$s are defined as follows. For W events with a reconstructed primary vertex, ϵ^{trk}_W is the efficiency for reconstructing a single TPC track which satisfies the track requirements in Sec. IV A, however for $Z \to e^+e^-$ events the tracking efficiency, ϵ^{trk}_Z, is the efficiency for reconstructing *two* TPC tracks satisfying those conditions. In comparing the reconstructed TPC track $1/p_T$ distributions between data and MC, a slightly worse resolution was seen in the data. This was accounted for by re-weighting the MC distributions to match the data. The uncertainty on the tracking efficiency was estimated from the error in this re-weighting resulting from the limited statistics of the data distribution.

Finally, the algorithm efficiency, ϵ^{algo}, is the fraction of events with one (two) reconstructed $e^\pm$ candidate TPC tracks, which satisfy the remaining W (Z) selection criteria. As discussed in Sec. IV, these remaining selection criteria include reconstruction of BEMC clusters, matching extrapolated track and cluster positions, isolation requirements, and finally the signed P_T-balance and pair of opposite charge-sign candidate requirements for W and Z events, respectively. A weak E_T^e dependence was observed in the algorithm efficiency for the $W \to e\nu$ MC due mainly to the efficiency of the $E_T^e/E_T^{\Delta\mathrm{R}<0.7}$ isolation cut being reduced at low E_T^e. Thus, an E_T^e-dependent algorithm efficiency correction was used in the computation of the $W^\pm$ cross sections. The uncertainty on ϵ^{algo}

was determined by varying the BEMC scale uncertainty, as was done for the trigger efficiency.

	$W^+ \to e^+ \nu_e$	$W^- \to e^- \bar{\nu}_e$	$Z \to e^+e^-$
ϵ^{trig}	0.857 ± 0.007	0.825 ± 0.007	0.968 ± 0.006
ϵ^{vert}	0.881 ± 0.005	0.886 ± 0.006	0.938 ± 0.006
ϵ^{trk}	0.741 ± 0.030	0.748 ± 0.031	0.511 ± 0.032
ϵ^{algo}	0.892 ± 0.024	0.892 ± 0.024	0.730 ± 0.024
ϵ^{tot}	0.498 ± 0.026	0.488 ± 0.026	0.338 ± 0.024

TABLE II. Summary of efficiency correction factors included in Eq. 7. The average values for the trigger and algorithm efficiencies for the $W^{\pm}$ analysis are given here, however an E_T^e-dependent correction was used for the measured cross section, as described in the text.

B. The Measured Fiducial Cross Sections

The fiducial cross sections are calculated according to Eq. 4, and the measured values are summarized in Tables III and IV for $W^{\pm}$ and Z respectively. The dominant uncertainty for both the W^+ and W^- cross sections comes from the systematic uncertainty in the measured luminosity of the data sample. The Z cross section measurement, however, is currently dominated by the statistical uncertainty.

	$W^+ \to e^+ \nu_e$				$W^- \to e^- \bar{\nu}_e$			
	value	stat	syst	lumi	value	stat	syst	lumi
N^{obs}	496	22.3	-	-	148	12.2	-	-
N^{bkgd}	36.6	3.5	$^{+5.4}_{-5.2}$	-	25.8	3.2	$^{+3.6}_{-2.8}$	-
ϵ^{tot}	0.498	0.006	0.025	-	0.488	0.007	0.025	-
L (pb^{-1})	13.2	0.2	-	1.7	13.2	0.2	-	1.7
σ^{fid} (pb)	70.0	3.5	3.5	9.1	19.2	2.1	1.1	2.5

TABLE III. Summary of input and measured values for the $W \to e\nu$ fiducial cross sections, with their statistical, systematic, and luminosity uncertainties. As noted in the text, an E_T^e-dependent efficiency correction factor is used for the cross section measurement, and only the average value is shown here.

C. The Acceptance Correction Factors

As stated previously, to determine the total cross sections, acceptance correction factors $A_{W(Z)}$, must be used to account for the fiducial and kinematic acceptance requirements of the analysis, which are defined at the beginning of Sec. VI. $A_{W(Z)}$ were calculated using the FEWZ program [29], which provides cross section calculations for W and Z boson production up to NNLO in pQCD. Table V lists the values of the acceptance factors using

	$Z \to e^+e^-$			
	value	stat	syst	lumi
N^{obs}	13	3.6	-	-
N^{bkgd}	0.1	0.1	$^{+1.3}_{-0.0}$	-
ϵ^{tot}	0.338	0.012	0.021	-
L (pb^{-1})	13.2	0.2	-	1.7
σ^{fid} (pb)	2.9	0.8	$^{+0.2}_{-0.3}$	0.4

TABLE IV. Summary of input and measured values for the $Z \to e^+e^-$ fiducial cross section, with their statistical, systematic, and luminosity uncertainties.

the MSTW 2008 [30] and CTEQ 6.6 [31] parton distribution function sets. The nominal values for the acceptance corrections, used in the total cross section measurements, were taken from the next-to-leading order (NLO) calculation using the MSTW08 PDF set. Theoretical uncertainties in the calculation of these factors arise from several sources, including differences between PDF sets, uncertainties within a PDF set, and uncertainties in the modeling of the production process.

	A_{W^+}	A_{W^-}	A_Z
LO MSTW08	0.591	0.444	0.377
NLO MSTW08	0.597	0.444	0.378
NNLO MSTW08	0.603	0.435	0.385
NLO CTEQ 6.6	0.592	0.430	0.370

TABLE V. Summary of acceptance values calculated with the FEWZ program. The NLO MSTW08 values are used for the total cross section calculations in Sec. VI D.

The uncertainty due to differences between PDF sets was taken to be the difference between the CTEQ 6.6 and MSTW08 acceptance values at NLO. Both groups provide error eigenvector PDF sets which were used to estimate the acceptance uncertainty, at the 90% confidence level, within each set. The average of the CTEQ 6.6 and MSTW08 error eigenvector uncertainty was taken to be the uncertainty due to the PDF itself. Finally, the uncertainty in the modeling of the production process was estimated by comparing the acceptance values from calculations with different orders of QCD corrections, using the MSTW08 PDF set. The maximum difference from the nominal value (NLO MSTW08) was taken as this final uncertainty contribution. Table VI summarizes the contributions to the uncertainties in the acceptance values. The individual contributions were added in quadrature to determine the total uncertainty for each acceptance factor. The A_{W^-} uncertainties are significantly larger than those for A_{W^+}, driven primarily by the PDF-related errors. This is expected, due to the larger uncertainties in the $\bar{u}$ and d quark PDFs with respect to those of the $\bar{d}$ and u quarks.

	$\delta A_{W^+}(\%)$	$\delta A_{W^-}(\%)$	$\delta A_Z(\%)$
Difference between PDFs	1.0	3.2	2.1
MSTW08 NLO error PDFs	0.9	2.7	1.2
CTEQ 6.6 NLO error PDFs	0.9	4.5	1.8
Calculation Order	1.0	2.0	1.9
Total	1.7	5.2	3.2

TABLE VI. Summary of the relative uncertainties in the acceptance correction factors, $A_{W(Z)}$, as computed by the FEWZ program.

D. The Measured Total Cross Sections

The total cross sections are calculated according to Eqs. 5 and 6, by dividing the measured fiducial cross sections by the acceptance correction factors determined in the previous section. The results for $pp \to W^{\pm}$ total production cross sections at $\sqrt{s} = 500$ GeV are the following:

$$\sigma^{tot}_{W^+} \cdot \mathrm{BR}(W^+ \to e^+ \nu_e) = 117.3 \pm 5.9(\mathrm{stat}) \pm 6.2(\mathrm{syst}) \pm 15.2(\mathrm{lumi})\ \mathrm{pb},$$

$$\sigma^{tot}_{W^-} \cdot \mathrm{BR}(W^- \to e^- \bar{\nu}_e) = 43.3 \pm 4.6(\mathrm{stat}) \pm 3.4(\mathrm{syst}) \pm 5.6(\mathrm{lumi})\ \mathrm{pb}.$$

The result for the $pp \to Z/\gamma^*$ total production cross section at $\sqrt{s} = 500$ GeV in the invariant mass range of $70 < m_{e^+e^-} < 110$ GeV/c^2 is

$$\sigma^{tot}_{Z/\gamma^*} \cdot \mathrm{BR}(Z/\gamma^* \to e^+e^-) = 7.7 \pm 2.1(\mathrm{stat}) \, ^{+0.5}_{-0.9}(\mathrm{syst}) \pm 1.0(\mathrm{lumi})\ \mathrm{pb}.$$

Figure 11 shows the measured total cross sections, multiplied by the respective branching ratios, in comparison with the theoretical predictions at NLO from the FEWZ program using the MSTW08 PDF set. Measurements from other experiments at the SpS̄, Tevatron, RHIC, and LHC are also shown as a function of $\sqrt{s}$ for comparison.

Theoretical predictions for the production cross sections computed by the FEWZ [29] and fully resummed RHICBOS [15] calculations are shown in Table VII. The theoretical uncertainties were determined for the FEWZ predictions using the 90% confidence level error eigenvector PDF sets; error eigenvector sets are not provided for the RHICBOS calculation. Variations in the strong coupling constant, α_s, from the associated error PDF sets were considered as well, but the uncertainties were found to be negligible compared to the uncertainties from the PDFs. The theoretical predictions agree well with the measured cross sections within the theoretical and experimental uncertainties. Interestingly, differences between the MSTW08 and CTEQ 6.6 PDF sets result in significant differences in the predicted cross sections at NLO.

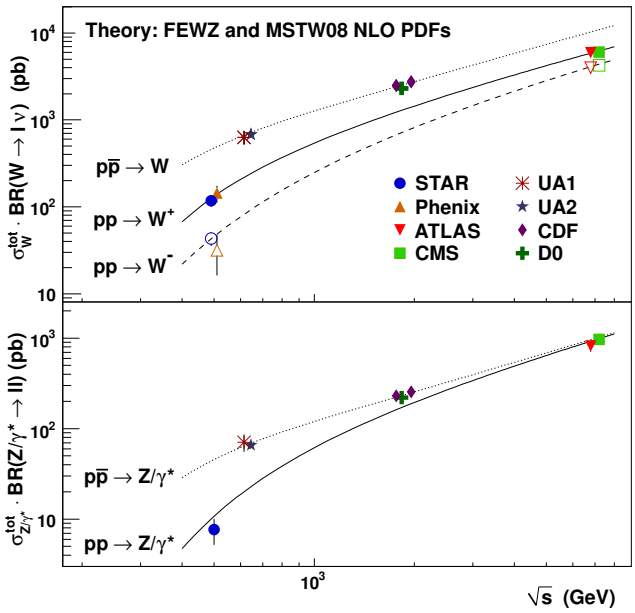

FIG. 11. (Color online) Measurements of W and Z/γ^* ($70 < m_{e^+e^-} < 110$ GeV/c^2) total cross sections times branching ratio versus center-of-mass energy. For the W cross sections in pp collisions, the closed symbols represent W^+ and the open symbols represent W^-. The theory curves are from the FEWZ program at NLO using the MSTW08 PDF set.

	$\sigma^{tot}_{W^+}$(pb)	$\sigma^{tot}_{W^-}$(pb)	$\sigma^{tot}_{Z} \cdot$(pb)
NLO MSTW08	132.4 ± 9.0	45.7 ± 3.6	10.8 ± 0.8
NNLO MSTW08	136.7 ± 9.5	48.1 ± 3.0	11.2 ± 0.8
NLO CTEQ 6.6	121.8 ± 8.8	41.1 ± 4.3	9.8 ± 0.8
Ressum. CTEQ 6.6	121.1	39.9	-

TABLE VII. Summary of total cross section (times branching ratio) theoretical predictions at $\sqrt{s} = 500$ GeV calculated with the FEWZ and RHICBOS programs. The Z/γ^* values are defined within the invariant mass range of $70 < m_{e^+e^-} < 110$ GeV/c^2.

VII. THE W CROSS SECTION RATIO

The W cross section ratio is defined as

$$R_W = \frac{\sigma^{fid}_{W^+}}{\sigma^{fid}_{W^-}} = \frac{N^{obs}_{W^+} - N^{bkgd}_{W^+}}{N^{obs}_{W^-} - N^{bkgd}_{W^-}} \cdot \frac{\epsilon^{tot}_{W^-}}{\epsilon^{tot}_{W^+}}. \quad (8)$$

If the small contributions from strange quarks are neglected, this ratio should be equal to [32]

$$R_W = \frac{u(x_1)\bar{d}(x_2) + \bar{d}(x_1)u(x_2)}{\bar{u}(x_1)d(x_2) + d(x_1)\bar{u}(x_2)}. \quad (9)$$

Measurements of the cross section ratio should therefore be sensitive to the flavor asymmetry of the antiquark sea in the Bjorken-x range $0.1 \lesssim x \lesssim 0.3$ probed at RHIC. Drell-Yan experiments [17, 18] have measured a large

asymmetry in this x range, and precision measurements of R_W at RHIC can provide independent constraints on the flavor asymmetry which are free from the assumption of charge symmetry required in Drell-Yan. Measurements of the lepton charge asymmetry at the LHC [33, 34] provide similar constraints on the quark and antiquark PDFs, though at significantly lower x due to the much higher energy of the collisions.

The W cross section ratio was measured in two $|\eta_e|$ regions, as this coarsely constrains the x of the partons involved in the W production. In each $|\eta_e|$ bin, the fiducial cross sections were computed using the same procedures described in Sec. VI, where the background and efficiencies were separately calculated for each charge and $|\eta_e|$ bin. The luminosity, and its sizable uncertainty, cancel in the cross section ratio, significantly reducing the systematic uncertainty, with respect to the W^+ and W^- cross sections independently.

	$R_W \pm$ (stat) $\pm$ (syst)
$\lvert\eta_e\rvert < 0.5$	$4.3 \pm 0.7 \pm 0.3$
$0.5 < \lvert\eta_e\rvert < 1.0$	$2.9 \pm 0.5 \pm 0.2$

TABLE VIII. (Color online) Measurements of the W cross section ratio, R_W, for the two $e^{\pm}$ pseudorapidity bins.

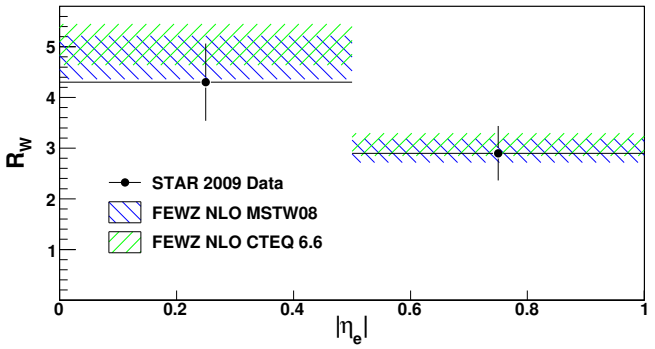

FIG. 12. (Color online) W cross section ratio, R_W, for the two $e^{\pm}$ pseudorapidity bins. Theory calculations at NLO from the FEWZ program using the MSTW08 and CTEQ 6.6 PDF sets (with 90% confidence level error eigenvector uncertainties) are shown for comparison.

Our results for the measured cross section ratio are listed in Table VIII. Figure 12 shows the cross section ratio as a function of $|\eta_e|$, where the statistical and systematic uncertainties of the data have been added in quadrature. Also displayed in Fig. 12 are theoretical calculations of the cross section ratio computed with the FEWZ program at NLO. Both the MSTW08 and CTEQ 6.6 PDF sets were used to compute the ratio; the error bands shown are the 90% confidence level error eigenvector uncertainties. The predictions agree with the measured values within the large uncertainties, which are dominated by the statistical precision of the W^- yield.

VIII. SUMMARY

We have presented measurements of the $W^+ \to e^+ \nu_e$ and $W^- \to e^- \bar{\nu}_e$ production cross sections in proton-proton collisions at $\sqrt{s} = 500$ GeV by the STAR detector at RHIC. A first measurement of the $Z/\gamma^* \to e^+e^-$ production cross section at $\sqrt{s} = 500$ GeV is also presented. Theoretical predictions based on pQCD calculations are in good agreement with the measured cross sections. In addition, a first measurement of the W cross section ratio is presented. Future high statistics measurements of the W cross section ratio at RHIC will provide a new means of studying the flavor asymmetry of the antiquark sea which is complementary to fixed-target Drell-Yan and LHC collider measurements.

ACKNOWLEDGMENTS

We thank the RHIC Operations Group and RCF at BNL, the NERSC Center at LBNL and the Open Science Grid consortium for providing resources and support. We are grateful to F. Petriello for useful discussions. This work was supported in part by the Offices of NP and HEP within the U.S. DOE Office of Science, the U.S. NSF, the Sloan Foundation, the DFG cluster of excellence 'Origin and Structure of the Universe' of Germany, CNRS/IN2P3, FAPESP CNPq of Brazil, Ministry of Ed. and Sci. of the Russian Federation, NNSFC, CAS, MoST, and MoE of China, GA and MSMT of the Czech Republic, FOM and NWO of the Netherlands, DAE, DST, and CSIR of India, Polish Ministry of Sci. and Higher Ed., Korea Research Foundation, Ministry of Sci., Ed. and Sports of the Rep. of Croatia, and RosAtom of Russia.

[1] C. Albajar *et al.* (UA1), Phys. Lett. **B198**, 271 (1987).
[2] C. Albajar *et al.* (UA1), Z. Phys. **C44**, 15 (1989).
[3] J. Alitti *et al.* (UA2), Z. Phys. **C47**, 11 (1990).
[4] J. Alitti *et al.* (UA2), Phys. Lett. **B276**, 365 (1992).
[5] F. Abe *et al.* (CDF), Phys. Rev. Lett. **76**, 3070 (1996), arXiv:hep-ex/9509010 [hep-ex].
[6] A. Abulencia *et al.* (CDF), J. Phys. **G34**, 2457 (2007), arXiv:hep-ex/0508029 [hep-ex].
[7] S. Abachi *et al.* (D0), Phys. Rev. Lett. **75**, 1456 (1995), arXiv:hep-ex/9505013 [hep-ex].
[8] B. Abbott *et al.* (D0), Phys. Rev. **D61**, 072001 (2000), arXiv:hep-ex/9906025 [hep-ex].

[9] M. Aggarwal *et al.* (STAR), Phys. Rev. Lett. **106**, 062002 (2011), arXiv:1009.0326 [hep-ex].

[10] A. Adare *et al.* (PHENIX), Phys. Rev. Lett. **106**, 062001 (2011), arXiv:1009.0505 [hep-ex].

[11] G. Aad *et al.* (ATLAS), JHEP **12**, 060 (2010), arXiv:1010.2130 [hep-ex].

[12] V. Khachatryan *et al.* (CMS), JHEP **01**, 080 (2011), arXiv:1012.2466 [hep-ex].

[13] S. Chatrchyan *et al.* (CMS), JHEP **10**, 132 (2011), arXiv:1107.4789 [hep-ex].

[14] D. de Florian and W. Vogelsang, Phys. Rev. **D81**, 094020 (2010), arXiv:1003.4533 [hep-ph].

[15] P. M. Nadolsky and C. Yuan, Nucl. Phys. **B666**, 31 (2003), arXiv:hep-ph/0304002 [hep-ph].

[16] A. Martin, R. Roberts, W. Stirling, and R. Thorne, Eur. Phys. J. **C28**, 455 (2003), arXiv:hep-ph/0211080 [hep-ph].

[17] A. Baldit *et al.* (NA51), Phys. Lett. **B332**, 244 (1994).

[18] R. Towell *et al.* (E866/NuSea), Phys. Rev. **D64**, 052002 (2001), arXiv:hep-ex/0103030 [hep-ex].

[19] K. H. Ackermann *et al.* (STAR), Nucl. Instrum. Meth. **A499**, 624 (2003).

[20] M. Anderson *et al.* (STAR), Nucl. Instrum. Meth. **A499**, 659 (2003).

[21] M. Beddo *et al.* (STAR), Nucl. Instrum. Meth. **A499**, 725 (2003).

[22] C. Allgower *et al.* (STAR), Nucl. Instrum. Meth. **A499**, 740 (2003).

[23] S. van der Meer, CERN-ISR-PO **68-31** (1968).

[24] P. Cameron *et al.*, Proceedings of the 1999 PAC.

[25] T. Sjostrand, S. Mrenna, and P. Z. Skands, JHEP **05**, 026 (2006), arXiv:hep-ph/0603175.

[26] R. Brun *et al.*, CERN-DD-78-2-REV (1978).

[27] B. Abelev *et al.* (STAR), Phys. Rev. Lett. **97**, 252001 (2006), arXiv:hep-ex/0608030 [hep-ex].

[28] G. J. Feldman and R. D. Cousins, Phys. Rev. **D57**, 3873 (1998), arXiv:physics/9711021 [physics.data-an].

[29] K. Melnikov and F. Petriello, Phys. Rev. **D74**, 114017 (2006), arXiv:hep-ph/0609070 [hep-ph].

[30] A. Martin, W. Stirling, R. Thorne, and G. Watt, Eur. Phys. J. **C63**, 189 (2009), arXiv:0901.0002 [hep-ph].

[31] P. M. Nadolsky *et al.*, Phys. Rev. **D78**, 013004 (2008), arXiv:0802.0007 [hep-ph].

[32] J. Peng and D. Jansen, Phys. Lett. **B354**, 460 (1995), arXiv:hep-ph/9508243 [hep-ph].

[33] G. Aad *et al.* (ATLAS), Phys. Lett. **B701**, 31 (2011), arXiv:1103.2929 [hep-ex].

[34] S. Chatrchyan *et al.* (CMS), JHEP **04**, 050 (2011), arXiv:1103.3470 [hep-ex].